Multi-parametric MRI can detect enhanced myelination in the Gli1$^{-/-}$ mouse brain

Choong H. Lee[1], Mara Holloman[2], James L. Salzer[2], Jiangyang Zhang[1]

[1] Bernard and Irene Schwartz Center for Biomedical Imaging, Department of Radiology, New York University School of Medicine, New York, NY 10016, USA

[2] Department of Neuroscience and Physiology, Neuroscience Institute, New York University School of Medicine, New York, NY 10016, USA

Abstract: 200 words

Main text: 3707 words

Corresponding to:

Jiangyang Zhang, Ph.D.

Center for Biomedical Imaging,

Department of Radiology,

New York University School of Medicine,

660 First Ave.

New York, NY 10016, USA

Jiangyang.zhang@nyulangone.org

Abstract (200 words)

Purpose: The ability of MRI-based markers to detect myelin in the brain is limited. This study investigated the potential of combining multiple MRI markers, each targeting distinct myelin properties, to improve myelin characterization.

Methods: We acquired ex vivo multiparametric MRI data at 7 Tesla from control and Gli1$^{-/-}$ mouse brains at postnatal day 10 (P10), which exhibits enhanced myelination in the corpus callosum, followed by myelin basic protein (MBP) stained immunohistochemistry.

Results: Although most MRI markers included in this study showed significant differences in the corpus callosum between control and Gli1$^{-/-}$, only fractional anisotropy (FA), mean diffusivity (MD), and T_2 had strong correlations with MBP signals. Partial least square regression (PSLR) based on MRI and MBP values from white matter regions suggested that T_2 had the highest contributions to myelin estimation. When both white and gray matter regions were included, inhomogeneous MT ratio and FA showed strong contributions.

Conclusion: This study demonstrates the efficacy of multi-parametric MRI in detecting enhanced myelination in the Gli1$^{-/-}$ mouse brain. T_2 and diffusion MRI parameters showed strong correlation with MBP signals in the genu of the corpus callosum at P10. The contribution of individual MRI parameter for detecting myelin can be evaluated using PLSR.

Keywords: MRI, myelin, mouse brain, Gli1, diffusion, relaxivity, magnetization transfer, partial least square regression

1. Introduction

Myelin is a multi-layered structure with lipid-rich cell membrane that is generated by the oligodendrocytes to insulate and support axons to facilitate rapid and efficient conduction of neuronal signals(1). The main chemical composition of myelin is lipid (~80 % of its dry mass) (2) and proteins (20% of its dry mass, including proteolipid protein (PLP) and myelin basic protein (MBP). Myelin pathology is commonly seen in neurological diseases, either with myelin as a direct target, such as in multiple sclerosis (MS) (1), leukodystrophy(3), or indirectly as in Alzheimer's disease (4,5), and is a central therapeutic target in primary demyelinating disorders. It is therefore important to develop methods for imaging myelin in order to detect myelin injury and monitor its repair, especially non-invasive imaging techniques.

MRI provides a myriad of tissue contrasts for the detection of myelin content and injury, including tissue relaxivity (e.g., T_1, T_2) (6-11), susceptibility (12-14), magnetization transfer (MT) (15-20), and diffusion (21-23). T_1 and T_2-MRI has long been used to survey myelin pathology in the brain (7,24), and the ratio between T_1-weighted and T_2-weighted MRI signals has been used as a measure of cortical myelin in the human brain (7). Furthermore, based on the distinct relaxivity properties of water compartments within or near myelin, the fraction of myelin water compartment can be estimated, which provides a more direct and sensitive marker for myelin (8,25) .

MT-MRI measures the transfer of magnetization between protons bounded to macromolecules (e.g. lipids and proteins) and free water protons (16,26,27). In a typical MT-MRI scan, a train of

off-resonance radiofrequency pulses is applied to saturate the bounded protons, and the saturation is then transferred to nearby free protons, effectively reducing the free protons' signal. MT MRI can be particularly useful in studying tissues with abundant macromolecules, including myelin in the CNS (15,26,28). Recently, inhomogeneous MT (ihMT), a variant of MT-MRI, presented its potential as a myelin marker with enhanced sensitivity to myelin lipid (29,30). Duhamel et al. showed a strong correlation between ihMT signals and the myelin content of several mouse brain structures as measured using fluorescence signals in the *plp-GFP* mouse brain, where the green fluorescent protein (GFP) is expressed under the transcriptional control of the myelin PLP regulatory sequences (31,32). We have demonstrated that ihMT-MRI can detect residual non-compact myelin in the hypomyelinated shiverer mouse brain better than conventional MT-MRI (33).

The distinct microstructural organization of myelin e.g., the multilammelar wrapping of the myelin sheath around an axon, makes it a restrictive barrier to water molecule diffusion, which can be detected by diffusion MRI. Early reports suggested mean diffusivity (MD) (34-36) and fractional anisotropy (FA) (34-37), two metrics derived from diffusion tensor imaging (DTI) (38,39), might be sensitive to myelin. Later, radial diffusivity (RD), which measures the extent of water diffusion perpendicular to the axon, has been demonstrated by Song et al. to be sensitive to demyelination (40). Diffusion kurtosis, which characterizes non-Gaussian diffusion property (41), has also been used to study myelin diseases (23,42,43). There has been a strong interest in using biophysical model-based analysis to extract the properties of specific cellular compartments (e.g., neurites and soma) from diffusion MRI signals (44,45). For instance, neurite and orientation dispersion density imaging (NODDI) (46) estimates the neurite density index

(NDI) and orientation dispersion index (ODI), which are relevant to myelin as myelin and axons are tightly coupled (47). It has also been shown that results from biophysical models can be combined with information from other contrast mechanisms to provide meaningful insights into myelin integrity and potential links to histology-based markers (e.g., g-ratio) (48-50).

The sensitivity and specificity of the above-mentioned and other MRI myelin markers, however, remain limited as demonstrated by a recent meta-analysis (51), mainly due to the indirect nature of MRI. This hinders the use of MRI to evaluate myelin pathology, particularly when confounding factors (e.g. inflammation, edema) are present (21). While many groups continue working on developing new sensitive techniques for myelin detection, an interesting question is whether we can combine multiple MRI markers to improve sensitivity and specificity (52). As previous studies benefitted from multiple contrasts mechanisms on different biophysical underpinnings of myelin (48,49,53), it would be ideal to combine the strengths of multiple translatable MRI contrasts, each targeting distinct aspect of myelin, to enhance the sensitivity and specificity to myelin. To achieve this goal, it is necessary to characterize multiple MRI markers with histological ground truth.

In this study, we acquired multi-parametric MRI data from the brains of Gli1 knockout (*Gli1*$^{-/-}$) mice. Loss of Gli1 promotes the differentiation of endogenous neural stem cells into oligodendrocytes thereby resulting in accelerated myelination of the forebrain compared to controls (54). We examined the correlations between the MRI parameters and MBP-stained histology in Gli1 null vs control brains. We used the partial least square regression (PSLR) to

remove collinearity among the MRI parameters and estimate the contribution of each MR marker to detection of enhanced myelination in this model.

2. Methods

2.1. Animals

The animal protocol has been approved by the institutional animal care and use committee at New York University Grossman School of Medicine. We crossed *Gli1*$^{+/-}$ heterozygous (hets) i.e., *Gli1*^{CreERT2} and *Gli1*^{nLacZ} to generate *Gli1*$^{CreERT2/nLacZ}$ i.e., *Gli1* null (*Gli1*$^{-/-}$) mice; *Gli*$^{+/-}$ hets served as controls. Postnatal day 10 (P10) het and null mice were perfusion-fixed with 4% paraformaldehyde (n = 3 in each group). We chose the P10 time point as *Gli1*$^{-/-}$ mice are substantially myelinated at this time in contrast to control mice which exhibit limited myelination. Dissected mouse brains were placed in 10 ml syringe filled with Fomblin (perfluoropolyether; Ausimont USA Inc.), which has no MRI visible proton, to match tissue susceptibility and prevent dehydration.

2.2. MRI Acquisition

All samples were imaged at room temperature using a 7 Tesla MRI system with a quadrature transmit volume coil (70 mm diameter) and a 4-channel receive-only phased array cryogenic probe (Bruker Biospin, Billerica, MA, USA).

For T_1 and T_2 MRI, we used the RAREVTR (Rapid Acquisition with Relaxation Enhancement and Variable Repetition time (TR)) (55) and MSME (Multi-Slice Multi-Echo) sequence with the parameters in Table 1. For MT-MRI, we used an offset frequency of 5 kHz for conventional MT-

MRI and 10 kHz for ihMT-MRI following previous reports by Prevost et al. (7). Images with no saturation pulse (M0) were acquired with images with positive/negative or dual-frequency saturation pulses (M_+, M_-, and $M_\pm$). MTR was calculated as: $MTR = 1 - \frac{M_+}{M_0}$, and ihMTR was calculated as: $ihMTR = ((M_+ + M_-) - 2M_\pm)/M_0$. Co-registered diffusion tensor data were acquired using a diffusion-weighted echo-planar imaging (DW-EPI) sequence. T_1/T_2, MT/ihMT, DW-EPI images were acquired using the scan parameters shown in **Table 1**.

A	TE (ms)	TR (ms)	Resolution (mm^3)	NEX/AT
T1-weighted RARE images	6.3	868, 1096, 1365, 1694, 2115, 2702, 3682, 7500	0.1 x 0.1 x 0.7	2/15 min
T2-weighted MSME images	7, 14, 21, 28, 34, 41, 48, 55, 62, 69, 76 83, 89, 96, 103, 110, 117, 124, 131, 138, 144, 151, 158, 165, 172	4000	0.1 x 0.1 x 0.7	2/40 min

B	TE (ms)	TR (ms)	Offset Freq (kHz)	Echo Train Length	Saturation Pulse	Pulsewidth/Bandwidth/Repetition time/# of pulses	Resolution (mm^3)	NEX/AT
MT	5.5	4000	5	6	Gaussian	1.83 ms/1.5 kHz/2.62ms/200	0.1 x 0.1 x 0.7 mm	4/22 min
ihMT	5.5	4000	10	6	Gaussian	1.83 ms/1.5 kHz/2.62ms/200	0.1 x 0.1 x 0.7 mm	4/1hr 14 min

C	TE (ms)	TR (ms)	Δ/δ (ms)	A0 images	Directions	B values (ss/mm^2)	Resolution (mm^3)	NEX/AT
Diffusion weighted EPI	33	5000	7/15	5	30	1000, 2500, 4000	0.1 x 0.1 x 0.7	2/15 min

Table 1: MR imaging parameters used in this study. Abbreviations are: AT: acquisition time; NEX: number of excitation; TE: echo time; TR: repetition time.

Image Analysis

MR images were reconstructed from raw data on the scanner console with trajectory correction (Paravision 6.0.1, Bruker Biospin, Billerica, MA, USA). T_1 and T_2 values were computed using the Image Sequence Analysis (ISA) Tool offered by Bruker Paravision. From

diffusion MRI data, diffusion tensor was calculated at each pixel along with the mean diffusivity (MD) and fractional anisotropy (FA) using MRtrix (www.mrtrix.org). The FA image was used for selecting the region of interest (ROI) including genu and splenium of corpus callosum (gcc and scc), external capsule (ec), cerebral peduncle (cp), internal capsule (ic) for white matter structures and motor cortex (mCX), sensory cortex (sCX), visual cortex (vCX), thalamus (TH), caudate putamen (CP), and hypothalamus (HY) for gray matter structures using ROIeditor (http://www.mristudio.org) due to its superior contrast for white matter structures even in the P10 mouse brains. From the corrected and combined DWIs, diffusion tensors and diffusion kurtosis tensors were obtained per voxel (41), their models were fitted using the standard kurtosis-fitting approach implemented in the Diffusion Kurtosis Imaging Matlab Toolbox (https://cai2r.net/resources/software/diffusion-kurtosis-imaging-matlab-toolbox) (56) and the following parameters were derived: MD, RD, FA, mean and radial kurtoses (MK/RK). NODDI metrics, NDI and ODI, were derived using the NODDI toolbox (http://www.nitrc.org/projects/noddi_toolbox) (46).

2.3. Histology

Post MRI *ex vivo* brains were dissected, cryo-protected in 30% sucrose solution and frozen embedded in OCT. Frozen brains were sectioned at 20 um thickness on a cryostat. Slides contain sections from the rostral to caudal regions of the corpus callosum. Slides were washed in PBS, incubated in 100% methanol at -20 °C for 10 minutes, incubated in blocking solution (10% goat serum diluted in 1X PBS, 1% BSA, 0.25% Triton-X100) for 1 hour at room temperature. Slides were incubated in the primary antibody (diluted in 1X PBS, 1% BSA, 0.25% Triton-X100) overnight at 4 °C. Slides were rinsed 3 x 5 minutes with PBS then incubated in the Alexa Fluor

secondary antibody for 1 hour at room temperature. Slides were rinsed 3 x 5 minutes with PBS and a final wash in distilled water then mounted with Fluoromount G mounting media and cover slipped. The primary antibody used for immunohistochemistry was chicken anti-MBP (Millipore, AB9348, 1:200); the secondary antibody used was goat anti-chicken (IgG 488, Jackson ImmunoResearch, 1:1000). Slides were imaged and acquired at 20x on Confocal Zeiss LSM 800 Fluorescence Microscope using Zeiss Zen blue software. Using imagej (57), the following ROIs were defined, e.g. for WM, genu (gcc), isthmus (icc), splenium of corpus callosum (scc), external capsule (ec), cerebral peduncle (cp), internal capsule (ic); for GM, motor cortex (mCX), sensory cortex (sCX), visual cortex (vCX), thalamus (TH), caudate putamen (CauP), hypothalamus (HY).

2.4. Partial Least Squares Regress (PLSR)

We used the function *plsregress* in Matlab® 9.6.0 (R2019a) to compute variable importance in projection (VIP) score, regression coefficients, and the percent of variance explained in the response variable (PCTVAR), etc. For each subject, the independent variables were the mean MRI markers from each ROI, and the response variable was the mean MBP signals in the corresponding ROI in histology from the same subject. Both variables were projected into a latent space, in which linear square regression was carried out. This approach reduces collinearity within the independent variables and dimension of the independent variables without reducing the prediction power (58).

2.5. Statistics

Statistical significance was determined using an unpaired Student's t-test with the threshold set at 0.05. All statistical tests were performed with Prism (GraphPad). All values in bar graphs indicate mean values and standard deviations.

3. **Results**

3.1 Multi-parametric MRI and histology of Gli1$^{-/-}$ mice:

We first examined the correlations between MRI markers to mean intensity values in MBP-stained histology. Fig. 1 and supplementary Fig. S1 show representative MBP-stained histology of Gli1 null (left, Gli1$^{-/-}$) and heterozygous (right, Gli1$^{+/-}$) mouse brains at P10 and maps of eleven MRI parameters at comparable locations from the same animal. Overall, the white matter (WM) and gray matter (GM) contrast in MRI were relatively low due to low myelin content in the P10 mouse brain (myelination begins at ~P8 in the mouse brain). T_1 and T_2 maps showed that the mouse corpus callosum (cc) at P10 had longer T_1 and T_2 values than the neighboring cortex. The cc had lower MTR values but higher ihMTR values than the cortex. In comparison, diffusion MRI markers showed better WM/GM contrasts, with higher FA, MK/RK, and NDI in and lower MD/RD and ODI in the cc than the cortex.

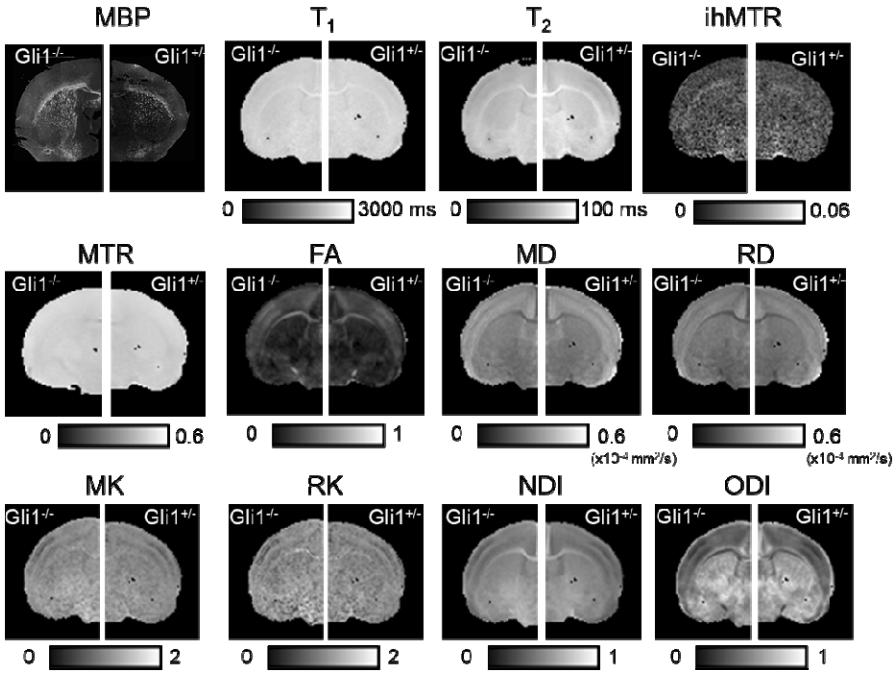

Fig.1. Representative axial MBP-stained histology of Gli1$^{-/-}$ and Gli1$^{+/-}$ mouse brains and corresponding MR parameter maps at the level of the genu of corpus callosum.

As we expected, MBP values measured in both the genu and splenium of the corpus callosum (gcc and scc, respectively) confirmed enhanced myelination in the Gli1$^{-/-}$ mouse brains compared to the Gli1$^{+/-}$ mouse brains at P10, and the difference was greater in gcc than scc (Fig. 2). T_2, MTR, ihMTR, and FA measurements showed significant differences between the Gli1$^{-/-}$ and Gli1$^{+/-}$ mouse brains in both the gcc and scc, whereas MD, RD, MK, and NDI only showed significant differences between the Gli1$^{-/-}$ and Gli1$^{+/-}$ mouse brains in the gcc. Interestingly, we found a significant difference in ODI in the scc but not in the gcc between the two groups of mice. No significant difference was found in T_1 and RK.

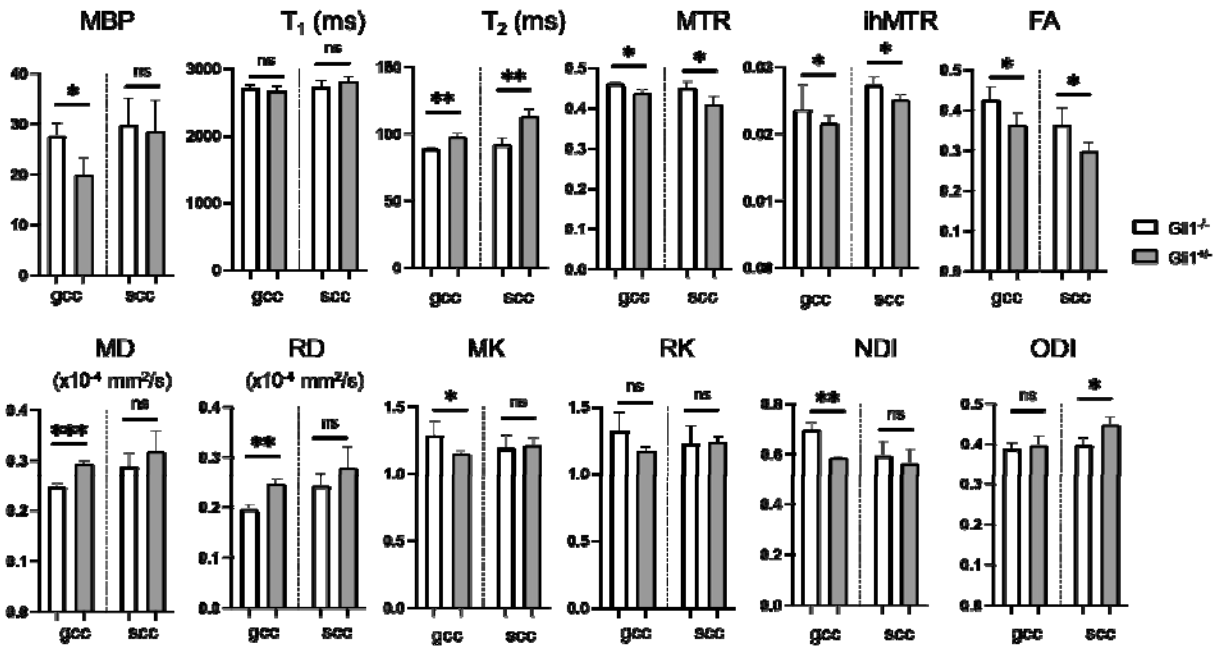

Fig.2. Quantitative analysis of MBP histology and MR parameter in gcc and scc in the Gli1$^{-/-}$ and Gli1$^{+/-}$ mouse brains**.** **/***/****: p□<□0.01/0.001/0.0001 by Student's t-test without corrections for multiple comparisons.

We then calculated the correlation between MBP signals and individual MR markers in the corpus callosum. In the gcc (Fig. 3), T_2 had the strongest correlation with MBP (R^2=0.88, p=0.01), and FA and MD showed relatively strong correlations with MBP (R^2=0.73, p=0.03, and R^2=0.76, p=0.02, respectively). ihMTR, MTR, MK, and T_1 had moderate but not significant correlations with MBP (R^2=0.32, p=0.24; R^2=0.43, p=0.16; R^2=0.46, p=0.14; and R^2=0.05, p=0.66, respectively). In addition, NDI had a strong correlation (R^2=0.80, p=0.02) while ODI has a weak correlation (R^2=0.2, p=0.37). In the scc, only MD showed relatively strong correlations with MBP (R^2=0.76, p=0.08, Supplementary Fig. S2).

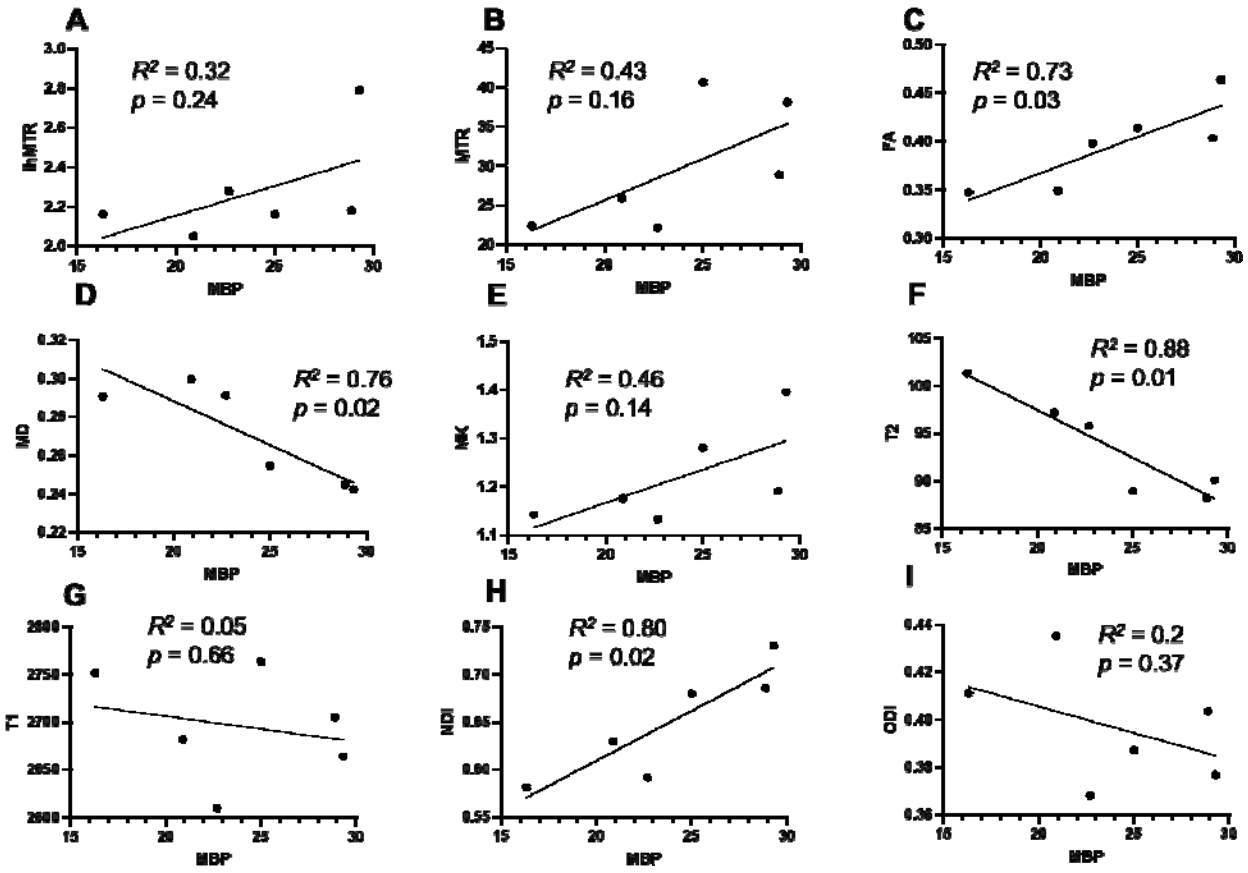

Fig.3. Correlation between MBP signals and MR parameters in the genu of corpus callosum (gcc) of Gli1$^{-/-}$ and Gli1$^{-/+}$ mouse brains.

When we included other ROIs in correlation analysis and averaged the results from both Gli1$^{-/-}$ and Gli1$^{+/-}$ mouse brains, we found that ihMTR, MTR, FA, MK, RK, and NDI had significant correlations with MBP signals when both GM and WM ROIs were considered (Fig. 4A). When only WM ROIs were considered (Fig. 4B), the R values of these markers were lower except MTR, whose R values increased from 0.18 to 0.68. We also examined the collinearity among the MRI markers in this mouse model based on measurements from WM and GM ROIs (Fig. 4). The correlation matrix in Fig. 4 indicates strong correlation among MK, RK, and NDI (R > 0.77) as

well as between MD and RD (R >0.85). The overall correlations in the GM-only correlation matrix were weaker than the former two cases (Fig. 4C).

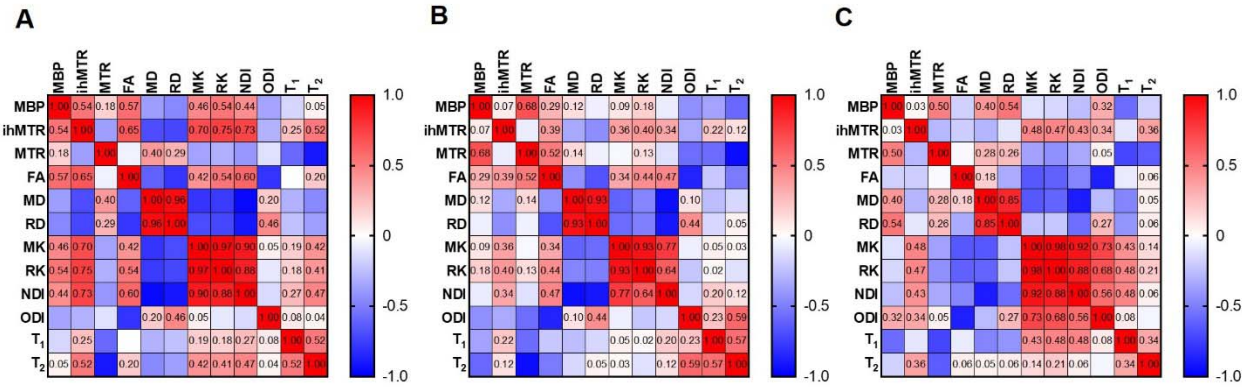

Fig.4. Correlation matrixes of multiple WM and GM ROIs in correlation analysis and averaged the results from both Gli1$^{-/-}$ and Gli1$^{+/-}$ mouse brains: WM and GM ROIs (A), WM ROIs (B) and GM ROIs (C).

3.2 PLSR and myelin estimation based on multiple markers

From each brain, mean MRI parameter values of 8 WM and 7 GM ROIs were included for the PLSR analysis. Based on the results in Fig. 4, we only included ihMTR, MTR, FA, MD, MK, ODI, T_1, and T_2, removing RD, RK, and NDI to minimize redundancy. At least 7 latent components were needed to explain approximately 60% variance of the MBP signals (Fig. 5A), supporting the inclusion of multiple MRI parameters. The resultant VIP scores implied that the MRI parameters with high contribution are ihMTR and FA (VIP score > 1), followed by MK and ODI, whose VIP score was slightly lower than one (Fig. 5B). When only WM ROIs were included for the PLSR analysis, slightly higher percentage in the variance of the MBP signals could be explained by the MRI parameters (Fig. 5C), and T_2 was the only parameter with a VIP score greater than one.

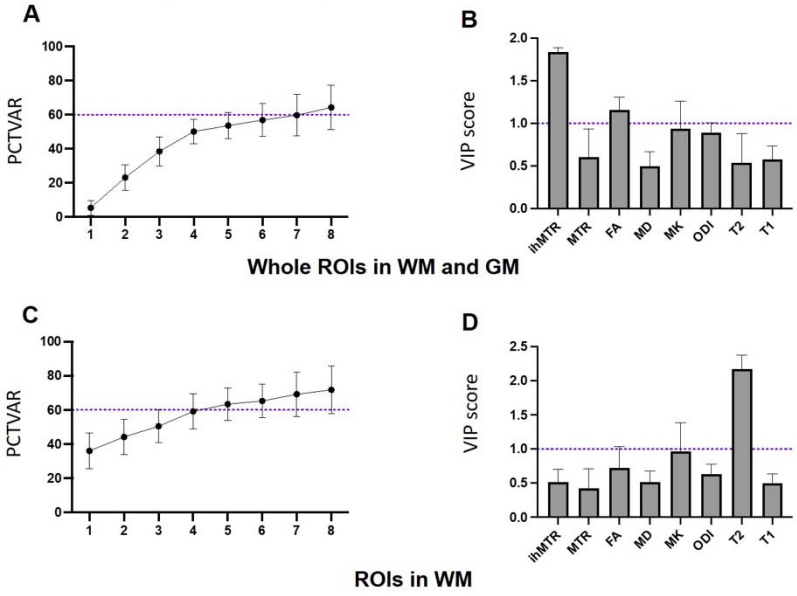

Fig.5. PLSR results showing the percentage of variance (PCTVAR) of the MBP signals that can be explained by the number of latent variables and the variable importance in projection (VIP) scores of each MRI parameters.

4 Discussion

This study used multi-parametric MRI and MBP-stained myelin histology from a mouse model of enhanced myelination to demonstrate the intricate relationship between MRI signals and CNS myelin. The Gli1 mouse model is different from mouse models commonly studied by MRI e.g., the cuprizone model (59) or EAE (60) as there is no inflammation or axonal injury in this model, therefore removing two common confounding factors. Although most MRI parameters included in this study showed significant changes in the corpus callosum between the Gli1$^{-/-}$ and Gli1$^{-/+}$ mouse brains (Fig. 2), only a subset of them had significant correlations with MBP-stained

histology (Fig. 3). Echoing a recent meta-analysis (51), our results demonstrated varying degrees of correlations between MRI parameters and myelin histology (Fig. 4), and PLSR results (Fig. 5) further suggesting that multiple MRI parameters are necessary to account for the variances observed in tissue MBP signals, i.e., the benefits of multi-parametric MRI.

4.1 Correlations between MRI parameters and MBP histology in the Gli1 mouse model

When both WM and GM structures were included (Fig. 4A), ihMTR were strongly correlated with MBP signals, diffusion MRI parameters showed moderate correlations, whereas T_1 and T_2 showed weak correlations, similar to results from the previous meta-analysis (51). However, when we examined WM and GM structures separately (Fig. 4B-C), MTR showed strong correlations, while diffusion MRI parameters showed less strong correlations. Among diffusion MRI parameters, NDI and MK presented strong correlations no matter whether the ROIs were grouped or not, which supports geometrical shapes and their density of neurites (axons, dendrites, etc) worked as a barrier against free water movement. These results also suggest that the relationship between MRI markers and MBP signals may not be linear and may depend on the underlying microstructures. For example, MTR showed a stronger correlation with MBP signals than ihMTR when examined in WM and GM ROIs alone (Fig. 4B and C), but once both WM and GM ROIs were evaluated together, ihMTR presented a stronger correlation with MBP signals (Fig. 4A), which warrants further investigation with more samples in the future.

Focusing on the corpus callosum to minimize differences in microstructural organization, we found significant correlations between MBP histology and several diffusion MRI parameters, including FA, MD, and NDI (Fig. 3), before corrections for multiple comparisons. It is possible

that these markers are associated with the density of myelinated axons, which form an effective restrictive barrier to water diffusion, as suggested by previous studies. Although MTR and ihMTR did not show significant correlations here, they generally increased with higher MBP signals as expected. The T_1 value of cc in both animal brain groups as a whole (2,734±60 ms) is in the range of reported values at the early age group of mice compared to adults at P57 (35,61). The observation that T_1 did not show significant sensitivity between these two groups may be attributed to the possibility that T_1 could potentially emerge as a more effective marker in the later stages of development (62). Although the limited number of animals in this study prevented us from statistically comparing the performances of these MRI parameters, the result suggests the possibility that diffusion MRI and T_2 parameters may be more sensitive to white matter myelin content at the early stage of myelination than MT parameters. The early myelin sheath may already restrict water molecule diffusion and chemical environment within white matter structure. This may not be true for later stage, when mature compact myelin has been formed.

4.2 How to identify the optimal myelin marker

Even though multiple MRI parameters are better than a single parameter, it is necessary to establish the contributions of individual markers for further optimization i.e., to pick the most useful ones and remove redundant or less sensitive ones. In this aspect, the PLSR handles collinearity among MRI parameters and provides important information on the contributions of each parameter. Even though the input MRI parameters cannot explain 100% of the observed variances in MBP signals, it is reasonable to expect certain variances in MBP signals coming from tissue processing and staining, which may be reduced in future studies by utilizing recent

advances in tissue clearing (63) and genetically modified mouse models with GFP co-expressed with selected myelin proteins (64,65). Choosing the optimal set of MRI parameters will require additional studies. Due to limited number of subjects included in this study, we compared PLSR results from WM only and WM+GM. In the WM only case, T_2 was the only parameter with VIP score higher than 1. This is not surprising, as T_2 signal showed strong correlation with MBP signals in the corpus callosum (Fig. 3). The strong correlation between T_2 signal and MBP signals primarily due to the sensitivity of T_2-weighted MRI to changes in water content and tissue characteristics, which are influenced by variations in myelin content and pathological conditions affecting the corpus callosum.

4.3. Limitations of the current study

This study has several limitations. Both the choice of *ex vivo* MRI, which is known to differ from *in vivo* MRI (66), and the early stage of myelination at P10, make it difficult to generalize the findings here to *in vivo* studies and mouse brains at later stages. In addition, there are other key aspects of myelin (e.g., myelin lipids) not captured by the MBP staining here, and several MRI myelin markers (e.g., myelin water fraction) were not included in this study. Future studies will be useful to further our understanding of optimal MRI-based myelin markers.

Even though we included a relatively large set of MRI parameters in this study, several important MRI-based myelin markers were left out due to practical reasons. One such marker is myelin water fraction from myelin water imaging, which has been shown to be a robust marker of remyelination in a clinical trial (67). In the P10 mouse brain, it is unknown whether compact myelin has formed at this stage and what the myelin water T_2 values are, it is challenging to estimate the fraction of myelin water compartment and will require further validation and

optimization. Quantitative Magnetization Transfer (qMT) has demonstrated its ability to effectively assess demyelination through the pool size ratio in a shiverer mouse model (68). This metric has shown strong correlations with histopathological findings in a rabbit model (69) and in post-mortem human brains affected by multiple sclerosis (MS) (34). Incorporating these advanced myelin markers in future studies will be a high priority.

Conclusion

Our results demonstrated that multi-parametric MRI is able to capture enhanced myelination in the brains of Gli1 mice – a model of early onset myelination. Based on MBP-stained myelin histology, T_2 and several diffusion MRI parameters showed strong correlation with MBP signals in the genu of the corpus callosum. Using PLSR, we were able to evaluate the contribution of individual MRI parameter for detecting myelin in the mouse brain at P10.

Acknowledgement

We would like to thank Jacob Brady for assisting sample preparation and histology. This study was supported by the National Institute of Health R01NS102904, R01HD074593, U24NS135568, and was performed at the Center of Advanced Imaging Innovation and Research (CAI2R, www.cai2r.net), a Biomedical Technology Resource Center supported by NIBIB with the award P41 EB017183.

References

1. Chang KJ, Redmond SA, Chan JR. Remodeling myelination: implications for mechanisms of neural plasticity. Nat Neurosci 2016;19(2):190-197.
2. O'Brien JS, Sampson EL. Lipid composition of the normal human brain: gray matter, white matter, and myelin. J Lipid Res 1965;6(4):537-544.
3. van der Knaap MS, Bugiani M. Leukodystrophies: a proposed classification system based on pathological changes and pathogenetic mechanisms. Acta Neuropathol 2017;134(3):351-382.
4. Depp C, Sun T, Sasmita AO, Spieth L, Berghoff SA, Nazarenko T, Overhoff K, Steixner-Kumar AA, Subramanian S, Arinrad S, Ruhwedel T, Mobius W, Gobbels S, Saher G, Werner HB, Damkou A, Zampar S, Wirths O, Thalmann M, Simons M, Saito T, Saido T, Krueger-Burg D, Kawaguchi R, Willem M, Haass C, Geschwind D, Ehrenreich H, Stassart R, Nave KA. Myelin dysfunction drives amyloid-beta deposition in models of Alzheimer's disease. Nature 2023;618(7964):349-357.
5. Chen JF, Liu K, Hu B, Li RR, Xin W, Chen H, Wang F, Chen L, Li RX, Ren SY, Xiao L, Chan JR, Mei F. Enhancing myelin renewal reverses cognitive dysfunction in a murine model of Alzheimer's disease. Neuron 2021;109(14):2292-2307 e2295.
6. Miot-Noirault E, Barantin L, Akoka S, Le Pape A. T2 relaxation time as a marker of brain myelination: experimental MR study in two neonatal animal models. J Neurosci Methods 1997;72(1):5-14.
7. Glasser MF, Goyal MS, Preuss TM, Raichle ME, Van Essen DC. Trends and properties of human cerebral cortex: correlations with cortical myelin content. Neuroimage 2014;93 Pt 2:165-175.
8. MacKay AL, Laule C. Magnetic Resonance of Myelin Water: An in vivo Marker for Myelin. Brain Plast 2016;2(1):71-91.
9. Laule C, Kozlowski P, Leung E, Li DK, Mackay AL, Moore GR. Myelin water imaging of multiple sclerosis at 7 T: correlations with histopathology. Neuroimage 2008;40(4):1575-1580.
10. Laule C, Vavasour IM, Leung E, Li DK, Kozlowski P, Traboulsee AL, Oger J, Mackay AL, Moore GR. Pathological basis of diffusely abnormal white matter: insights from magnetic resonance imaging and histology. Mult Scler 2011;17(2):144-150.

11. Laule C, Leung E, Lis DK, Traboulsee AL, Paty DW, MacKay AL, Moore GR. Myelin water imaging in multiple sclerosis: quantitative correlations with histopathology. Mult Scler 2006;12(6):747-753.
12. Lee J, Shmueli K, Kang BT, Yao B, Fukunaga M, van Gelderen P, Palumbo S, Bosetti F, Silva AC, Duyn JH. The contribution of myelin to magnetic susceptibility-weighted contrasts in high-field MRI of the brain. Neuroimage 2012;59(4):3967-3975.
13. Shin HG, Lee J, Yun YH, Yoo SH, Jang J, Oh SH, Nam Y, Jung S, Kim S, Fukunaga M, Kim W, Choi HJ, Lee J. chi-separation: Magnetic susceptibility source separation toward iron and myelin mapping in the brain. Neuroimage 2021;240:118371.
14. Duyn J. MR susceptibility imaging. J Magn Reson 2013;229:198-207.
15. Vavasour IM, Laule C, Li DK, Traboulsee AL, MacKay AL. Is the magnetization transfer ratio a marker for myelin in multiple sclerosis? J Magn Reson Imaging 2011;33(3):713-718.
16. Henkelman RM, Stanisz GJ, Graham SJ. Magnetization transfer in MRI: a review. NMR Biomed 2001;14(2):57-64.
17. Sled JG, Pike GB. Quantitative imaging of magnetization transfer exchange and relaxation properties in vivo using MRI. Magn Reson Med 2001;46(5):923-931.
18. Sled JG. Modelling and interpretation of magnetization transfer imaging in the brain. Neuroimage 2018;182:128-135.
19. Rademacher J, Engelbrecht V, Burgel U, Freund H, Zilles K. Measuring in vivo myelination of human white matter fiber tracts with magnetization transfer MR. Neuroimage 1999;9(4):393-406.
20. Xydis V, Astrakas L, Zikou A, Pantou K, Andronikou S, Argyropoulou MI. Magnetization transfer ratio in the brain of preterm subjects: age-related changes during the first 2 years of life. Eur Radiol 2006;16(1):215-220.
21. Rahmanzadeh R, Lu PJ, Barakovic M, Weigel M, Maggi P, Nguyen TD, Schiavi S, Daducci A, La Rosa F, Schaedelin S, Absinta M, Reich DS, Sati P, Wang Y, Bach Cuadra M, Radue EW, Kuhle J, Kappos L, Granziera C. Myelin and axon pathology in multiple sclerosis assessed by myelin water and multi-shell diffusion imaging. Brain 2021;144(6):1684-1696.

22. Harkins KD, Does MD. Simulations on the influence of myelin water in diffusion-weighted imaging. Phys Med Biol 2016;61(13):4729-4745.
23. Guglielmetti C, Veraart J, Roelant E, Mai Z, Daans J, Van Audekerke J, Naeyaert M, Vanhoutte G, Delgado YPR, Praet J, Fieremans E, Ponsaerts P, Sijbers J, Van der Linden A, Verhoye M. Diffusion kurtosis imaging probes cortical alterations and white matter pathology following cuprizone induced demyelination and spontaneous remyelination. Neuroimage 2016;125:363-377.
24. Mottershead JP, Schmierer K, Clemence M, Thornton JS, Scaravilli F, Barker GJ, Tofts PS, Newcombe J, Cuzner ML, Ordidge RJ, McDonald WI, Miller DH. High field MRI correlates of myelin content and axonal density in multiple sclerosis--a post-mortem study of the spinal cord. J Neurol 2003;250(11):1293-1301.
25. MacKay A, Whittall K, Adler J, Li D, Paty D, Graeb D. In vivo visualization of myelin water in brain by magnetic resonance. Magn Reson Med 1994;31(6):673-677.
26. Schmierer K, Scaravilli F, Altmann DR, Barker GJ, Miller DH. Magnetization transfer ratio and myelin in postmortem multiple sclerosis brain. Ann Neurol 2004;56(3):407-415.
27. Wolff SD, Balaban RS. Magnetization transfer contrast (MTC) and tissue water proton relaxation in vivo. Magn Reson Med 1989;10(1):135-144.
28. Hakkarainen H, Sierra A, Mangia S, Garwood M, Michaeli S, Grohn O, Liimatainen T. MRI relaxation in the presence of fictitious fields correlates with myelin content in normal rat brain. Magn Reson Med 2016;75(1):161-168.
29. Varma G, Duhamel G, de Bazelaire C, Alsop DC. Magnetization transfer from inhomogeneously broadened lines: A potential marker for myelin. Magn Reson Med 2015;73(2):614-622.
30. Varma G, Girard OM, Prevost VH, Grant AK, Duhamel G, Alsop DC. Interpretation of magnetization transfer from inhomogeneously broadened lines (ihMT) in tissues as a dipolar order effect within motion restricted molecules. Journal of Magnetic Resonance 2015;260:67-76.
31. Duhamel G, Prevost VH, Cayre M, Hertanu A, McHinda S, Carvalho VN, Varma G, Durbec P, Alsop DC, Girard OM. Validating the sensitivity of inhomogeneous magnetization transfer (ihMT) MRI to myelin with fluorescence microscopy. Neuroimage 2019;199:289-303.

32. Spassky N, Olivier C, Cobos I, LeBras B, Goujet-Zalc C, Martinez S, Zalc B, Thomas JL. The early steps of oligodendrogenesis: insights from the study of the plp lineage in the brain of chicks and rodents. Dev Neurosci 2001;23(4-5):318-326.
33. Lee CH, Walczak P, Zhang J. Inhomogeneous magnetization transfer MRI of white matter structures in the hypomyelinated shiverer mouse brain. Magn Reson Med 2022;88(1):332-340.
34. Schmierer K, Wheeler-Kingshott CA, Tozer DJ, Boulby PA, Parkes HG, Yousry TA, Scaravilli F, Barker GJ, Tofts PS, Miller DH. Quantitative magnetic resonance of postmortem multiple sclerosis brain before and after fixation. Magn Reson Med 2008;59(2):268-277.
35. Thiessen JD, Zhang Y, Zhang H, Wang L, Buist R, Del Bigio MR, Kong J, Li XM, Martin M. Quantitative MRI and ultrastructural examination of the cuprizone mouse model of demyelination. NMR Biomed 2013;26(11):1562-1581.
36. Yano R, Hata J, Abe Y, Seki F, Yoshida K, Komaki Y, Okano H, Tanaka KF. Quantitative temporal changes in DTI values coupled with histological properties in cuprizone-induced demyelination and remyelination. Neurochem Int 2018;119:151-158.
37. Wendel KM, Lee JB, Affeldt BM, Hamer M, Harahap-Carrillo IS, Pardo AC, Obenaus A. Corpus Callosum Vasculature Predicts White Matter Microstructure Abnormalities after Pediatric Mild Traumatic Brain Injury. J Neurotrauma 2018;36(1):152-164.
38. Basser PJ, Mattiello J, LeBihan D. MR diffusion tensor spectroscopy and imaging. Biophys J 1994;66(1):259-267.
39. Mori S, Zhang J. Principles of diffusion tensor imaging and its applications to basic neuroscience research. Neuron 2006;51(5):527-539.
40. Song SK, Yoshino J, Le TQ, Lin SJ, Sun SW, Cross AH, Armstrong RC. Demyelination increases radial diffusivity in corpus callosum of mouse brain. Neuroimage 2005;26(1):132-140.
41. Jensen JH, Helpern JA, Ramani A, Lu H, Kaczynski K. Diffusional kurtosis imaging: the quantification of non-gaussian water diffusion by means of magnetic resonance imaging. Magn Reson Med 2005;53(6):1432-1440.

42. Kelm ND, West KL, Carson RP, Gochberg DF, Ess KC, Does MD. Evaluation of diffusion kurtosis imaging in ex vivo hypomyelinated mouse brains. Neuroimage 2016;124(Pt A):612-626.
43. Praet J, Manyakov NV, Muchene L, Mai Z, Terzopoulos V, de Backer S, Torremans A, Guns PJ, Van De Casteele T, Bottelbergs A, Van Broeck B, Sijbers J, Smeets D, Shkedy Z, Bijnens L, Pemberton DJ, Schmidt ME, Van der Linden A, Verhoye M. Diffusion kurtosis imaging allows the early detection and longitudinal follow-up of amyloid-beta-induced pathology. Alzheimers Res Ther 2018;10(1):1.
44. Fieremans E, Jensen JH, Helpern JA. White matter characterization with diffusional kurtosis imaging. Neuroimage 2011;58(1):177-188.
45. Hansen B, Khan AR, Shemesh N, Lund TE, Sangill R, Eskildsen SF, Ostergaard L, Jespersen SN. White matter biomarkers from fast protocols using axially symmetric diffusion kurtosis imaging. NMR Biomed 2017;30(9):e3741.
46. Zhang H, Schneider T, Wheeler-Kingshott CA, Alexander DC. NODDI: practical in vivo neurite orientation dispersion and density imaging of the human brain. Neuroimage 2012;61(4):1000-1016.
47. Qian W, Khattar N, Cortina LE, Spencer RG, Bouhrara M. Nonlinear associations of neurite density and myelin content with age revealed using multicomponent diffusion and relaxometry magnetic resonance imaging. Neuroimage 2020;223:117369.
48. Stikov N, Perry LM, Mezer A, Rykhlevskaia E, Wandell BA, Pauly JM, Dougherty RF. Bound pool fractions complement diffusion measures to describe white matter micro and macrostructure. Neuroimage 2011;54(2):1112-1121.
49. Stikov N, Campbell JS, Stroh T, Lavelee M, Frey S, Novek J, Nuara S, Ho MK, Bedell BJ, Dougherty RF, Leppert IR, Boudreau M, Narayanan S, Duval T, Cohen-Adad J, Picard PA, Gasecka A, Cote D, Pike GB. In vivo histology of the myelin g-ratio with magnetic resonance imaging. Neuroimage 2015;118:397-405.
50. Jung W, Lee J, Shin HG, Nam Y, Zhang H, Oh SH, Lee J. Whole brain g-ratio mapping using myelin water imaging (MWI) and neurite orientation dispersion and density imaging (NODDI). Neuroimage 2018;182:379-388.
51. Mancini M, Karakuzu A, Cohen-Adad J, Cercignani M, Nichols TE, Stikov N. An interactive meta-analysis of MRI biomarkers of myelin. Elife 2020;9:e61523.

52. Patel Y, Shin J, Drakesmith M, Evans J, Pausova Z, Paus T. Virtual histology of multi-modal magnetic resonance imaging of cerebral cortex in young men. Neuroimage 2020;218:116968.
53. Mangeat G, Govindarajan ST, Mainero C, Cohen-Adad J. Multivariate combination of magnetization transfer, T2* and B0 orientation to study the myelo-architecture of the in vivo human cortex. Neuroimage 2015;119:89-102.
54. Samanta J, Grund EM, Silva HM, Lafaille JJ, Fishell G, Salzer JL. Inhibition of Gli1 mobilizes endogenous neural stem cells for remyelination. Nature 2015;526(7573):448-452.
55. Hennig J, Nauerth A, Friedburg H. RARE imaging: a fast imaging method for clinical MR. Magn Reson Med 1986;3(6):823-833.
56. Veraart J, Sijbers J, Sunaert S, Leemans A, Jeurissen B. Weighted linear least squares estimation of diffusion MRI parameters: strengths, limitations, and pitfalls. Neuroimage 2013;81:335-346.
57. Schneider CA, Rasband WS, Eliceiri KW. NIH Image to ImageJ: 25 years of image analysis. Nat Methods 2012;9(7):671-675.
58. Yoshida K, Shimizu Y, Yoshimoto J, Takamura M, Okada G, Okamoto Y, Yamawaki S, Doya K. Prediction of clinical depression scores and detection of changes in whole-brain using resting-state functional MRI data with partial least squares regression. PLoS One 2017;12(7):e0179638.
59. Matsushima GK, Morell P. The neurotoxicant, cuprizone, as a model to study demyelination and remyelination in the central nervous system. Brain pathology (Zurich, Switzerland) 2001;11(1):107-116.
60. Constantinescu CS, Farooqi N, O'Brien K, Gran B. Experimental autoimmune encephalomyelitis (EAE) as a model for multiple sclerosis (MS). Br J Pharmacol 2011;164(4):1079-1106.
61. van de Ven RC, Hogers B, van den Maagdenberg AM, de Groot HJ, Ferrari MD, Frants RR, Poelmann RE, van der Weerd L, Kiihne SR. T(1) relaxation in in vivo mouse brain at ultra-high field. Magn Reson Med 2007;58(2):390-395.

62. Eminian S, Hajdu SD, Meuli RA, Maeder P, Hagmann P. Rapid high resolution T1 mapping as a marker of brain development: Normative ranges in key regions of interest. PLoS One 2018;13(6):e0198250.
63. Richardson DS, Guan W, Matsumoto K, Pan C, Chung K, Erturk A, Ueda HR, Lichtman JW. Tissue Clearing. Nat Rev Methods Primers 2021;1(1):84.
64. Hughes EG, Orthmann-Murphy JL, Langseth AJ, Bergles DE. Myelin remodeling through experience-dependent oligodendrogenesis in the adult somatosensory cortex. Nat Neurosci 2018;21(5):696-706.
65. Mallon BS, Shick HE, Kidd GJ, Macklin WB. Proteolipid promoter activity distinguishes two populations of NG2-positive cells throughout neonatal cortical development. J Neurosci 2002;22(3):876-885.
66. Roebroeck A, Miller KL, Aggarwal M. Ex vivo diffusion MRI of the human brain: Technical challenges and recent advances. NMR Biomed 2019;32(4):e3941.
67. Caverzasi E, Papinutto N, Cordano C, Kirkish G, Gundel TJ, Zhu A, Akula AV, Boscardin WJ, Neeb H, Henry RG, Chan JR, Green AJ. MWF of the corpus callosum is a robust measure of remyelination: Results from the ReBUILD trial. Proc Natl Acad Sci U S A 2023;120(20):e2217635120.
68. Ou X, Sun SW, Liang HF, Song SK, Gochberg DF. The MT pool size ratio and the DTI radial diffusivity may reflect the myelination in shiverer and control mice. NMR Biomed 2009;22(5):480-487.
69. Drobyshevsky A, Synowiec S, Goussakov I, Lu J, Gascoigne D, Aksenov DP, Yarnykh V. Temporal trajectories of normal myelination and axonal development assessed by quantitative macromolecular and diffusion MRI: Ultrastructural and immunochemical validation in a rabbit model. Neuroimage 2023;270:119974.
70. Harrison NA, Cooper E, Dowell NG, Keramida G, Voon V, Critchley HD, Cercignani M. Quantitative Magnetization Transfer Imaging as a Biomarker for Effects of Systemic Inflammation on the Brain. Biol Psychiatry 2015;78(1):49-57.